University of California, San Diego UCSD-CER-06-08

Manuscripts of Papers from the UCSD PISCES Program

Presented at the 17th Plasma-Surface Interactions Conference,
May 22-26, 2006, Hefei, China.

G. Antar, M. J. Baldwin D. Buchenauer, R.A. Causey, W.M. Clift, R.P. Doerner, C. Holland D. Nishijima, R. Seraydarian
K. Schmid, G. R. Tynan, J. H. Yu, and Z. Yan

Center for Energy Research
University of California, San Diego
9500 Gilman Drive
La Jolla, CA 92093-0420

This Report contains manuscripts of the following papers which were presented at the 17th International Conference on Plasma-Surface Interactions, held May 2006 in Hefei, China. Upon completion of their review, these papers will appear in a future edition of the Journal of Nuclear Materials.

1) **The implications of mixed-material plasma-facing surfaces**, R.P. Doerner (review)

2) **Parametric studies of carbon erosion mitigation dynamics in beryllium seeded deuterium plasmas,** D. Nishijima, M.J. Baldwin, R.P. Doerner and R. Seraydarian

3) **Examination of the velocity time-delay-estimation technique** J. H. Yu, C. Holland, G. R. Tynan, G. Antar, Z. Yan

4) **Be-W alloy formation in static and divertor-plasma simulator** M.J. Baldwin, D. Buchenauer, R. P. Doerner, R.A. Causey, D. Nishijima, W.M. Clift, and K. Schmid

The implications of mixed-material plasma-facing surfaces

R. P. Doerner

University of California at San Diego, 9500 Gilman Dr., La Jolla, CA. 92093-0417 USA

Abstract

In all plasma confinement devices, material eroded from plasma-facing surfaces will be transported and redeposited at other, sometimes remote, locations. If the plasma facing material in a device consists of more than a single element there is a high probability that the composition of the plasma-facing surfaces will evolve over time and may exhibit plasma interaction properties much different from the originally installed material. These plasma-created materials, or mixed materials, are the subjects of this review paper which focuses on the ITER relevant mix of materials, namely carbon, tungsten and beryllium. Knowledge concerning the formation conditions, erosion behavior and hydrogen isotope retention properties of each binary combination of materials is described. Where available information concerning tertiary combinations of materials is discussed.

PACS: 52.40.Hf

JNM Keywords: Plasma Material Interactions, Surface Effects, Beryllium, Carbon, Tungsten

PSI-17 Keywords: ITER, Erosion and Deposition, Chemical erosion, Co-deposition, Deuterium Inventory

Author address: Center for Energy Research

University of California at San Diego

9500 Gilman Dr.

Mail code: 0417

La Jolla, CA. 92093-0417

USA

Author e-mail: rdoerner@ucsd.edu

INTRODUCTION

The plasma facing surfaces provide the boundary conditions that govern the performance of any magnetically confined plasma device. The importance of these material surfaces will continue to increase as devices push toward higher and higher power and longer discharge duration. In machines that operate using a mixture of deuterium and tritium fuel, many safety aspects of operational capability will be determined by the behavior of the plasma-facing components and materials. For these reasons, the designers of the ITER project [1] have settled on a multi-material solution for their plasma-facing surfaces.

Unfortunately, the properties of the materials used in design calculations are usually the values associated with the ‘as-received’ material. In the proximity of high temperature plasma, material erodes from plasma-facing materials in one location and is transported to other locations throughout the device. The transported material may then be deposited on, or implanted into, other materials. In 1978, S. A. Cohen succinctly described this process [2] as “The wall may be eroded due to a variety of possible mechanisms which generate plasma impurities, and subsequent plasma transport of impurities may deposit material onto the wall. This modified surface of the wall is the wall component subjected to subsequent plasma-wall interactions; it is both a source and sink of plasma impurities and the working gas.” The term ‘mixed material’ has recently been coined to describe the resultant, plasma-created surface. Even though the importance of this issue was recognized almost three decades ago, detailed investigations of plasma interactions with surfaces composed of more than a single element began only during the last decade or so.

Although plasma altered surfaces have been observed in many confinement devices, once their compositions have been characterized, they have been largely ignored. The exceptions to this general statement seem to be those machines that have operated with a mixture of deuterium and tritium (D/T) fuel. The primary reason for the increased attention in D/T machines was the need to understand the tritium retention locations and characteristics throughout the devices. In the late 1980s, the term ‘tokamakium’ was used to refer to plasma created mixed-material surfaces found in TFTR [3]. Although TFTR was primarily an all-carbon machine, the impurity content and morphology of the mixed-material surfaces was found to reflect changes in the operational history of the device.

The other major D/T facility, JET, has also spent considerable effort on understanding the behavior of mixed-material surfaces [4-6]. In the JET device both carbon and beryllium were used together as plasma-facing materials and the resultant surfaces show considerable mixing between the two elements. Again, compositional changes in the depth profiles of the mixed-material surfaces can be correlated to the operational history of the machine [7]. The interrelated nature of the machine performance and the resultant plasma-facing surfaces indicates the importance of predicting the behavior of mixed-material surfaces in ITER prior to operating the device, both for facility safety requirements, as well as from the point of view of plasma performance and the achievement of the goals of the overall ITER project.

The conclusions derived from many active areas of research are needed to be able to accurately predict which mixed-materials surfaces will form in which regions of the ITER plasma-facing surfaces. The creation of mixed-material surfaces will depend on many factors that determine the arrival and loss rate of material from those surfaces [8]. In

order to know the arrival rate of an impurity species in the plasma at a given surface, one must understand the transport properties of the scrape-off layer (SOL) plasma. Edge plasma turbulence induces cross-field transport, resulting in both diffusive-like and convective plasma transport into and through the SOL region [9]. The magnitude of convectively transported flux to the first wall, commonly called blob transport [10], is actively being investigated. In addition, large SOL plasma flows have been measured but not yet explained in several plasma confinement machines [8]. Finally, erosion terms due to asymmetries and off-normal events, such as ELMs [11], also contribute to the distribution of impurities throughout the ITER vessel.

In spite of the large uncertainties associated with the locations where mixed materials will form in ITER, it can be predicted with some certainty that mixed-material surfaces will occur. Data on the characteristics and behavior of mixed-material surfaces is urgently needed by the ITER design team to try to anticipate and possibly mitigate any undesirable effects. Since ITER is presently designed with a beryllium first wall, tungsten armor in the baffle and divertor regions, and carbon strike point plates, this paper focuses on the mixed-material characteristics of these three materials. The present understanding of each of the binary systems, C/W, Be/C and Be/W, is described, including a discussion of the added complexity of tertiary systems incorporating oxygen into the mix. For each system, the formation conditions, the erosion characteristics and the hydrogen isotope retention properties of the mixed materials are described.

Carbon/Tungsten System

The carbon-tungsten mixed-material system is probably the most widely studied system, both experimentally and computationally. In 1991, experiments detected an interesting and unexpected reversal in the mass loss from room temperature tungsten samples bombarded with carbon ion beams at normal incidence [12]. Kinetics based Monte-Carlo codes using a binary collision approximation (BCA), such as TRIDYN [13] and EDDY [14], have had success predicting the sputtering behavior of tungsten surfaces exposed to such a flux of energetic carbon ions. The models track the changes in the composition of the implantation zone due to the bombardment of carbon ions. During the stopping process of the carbon ions, tungsten atoms can be sputtered from the initially pristine tungsten surface. The surface recession due to sputtering effectively acts to move the implanted carbon toward the surface. After some fluence, the initially implanted carbon ions will become part of the composition of the surface layer.

Once initially implanted carbon ions reach the new surface in the model several effects occur which change the interaction of the incoming carbon with the now mixed-material surface. First, the reflection probability of the incoming ions decreases due to a decrease in the mass difference between the projectile and the ‘average’ target species. The mass loss of tungsten from the surface then decreases as the concentration of surface carbon increases which is of course coupled to an increase in the loss rate of carbon from the surface. However, since the self-sputtering yield of carbon at normal incidence is always below unity [15], the overall mass of the sample begins to increase. At sufficiently large fluence, the sample will begin to experience a net mass gain.

The effect of the incident angle of the carbon ions can be used to verify the understanding obtained from the model. By simply increasing the angle between the

incident ions and the surface normal, one can obtain a condition where the self-sputtering yield of carbon is larger than unity. Under such condition, both the experiment and the model show a continuous decrease in the mass of bombarded tungsten samples [12].

To properly predict the behavior of material systems in confinement devices, it is necessary to include effects that become important at elevated surface temperature. While temperature dependent effects are not included in these models, it is possible to couple the kinetcis models with subroutines that allow variations of the composition in surface layers to include effects, such as diffusion. This has been done [16-18] and the comparison of the model to experiments can be quite good. However, in each case the diffusion coefficients needed to reproduce the experimental data are smaller than the values prescribed in the literature [see list of references in 16].

One possible explanation for this behavior begins to shed light on the complexity of modeling plasma created mixed-material surfaces. In addition to activating diffusion at elevated sample temperature, reactions between the substrate material and the implanted carbon species occur, resulting in the formation of carbides. Depending on the substrate material involved, carbides with different bonding characteristics are observed [19]. Carbides that form ionic bonds, such as Be_2C, are very stable against diffusion of carbon. Similarly, but to a somewhat lesser extent, covalent carbides, such as SiC, also resist diffusion of the carbon component. However, carbides that form with carbon filling the regions in the close packed metal lattice, such as WC, tend to be more favorable for diffusion since for diffusion to occur no direct bonds between the metal and the carbon must be broken in the process [19]. Effects such as this demonstrate the importance of including chemical effects in the models to accurately predict the behavior of plasma-

exposed surfaces. It may not be adequate to search the literature for data obtained during measurements performed under equilibrium, or trace concentration, conditions and then attempt to use that data to model the behavior of materials exposed to plasma where the situation may be far from equilibrium and the concentrations of species may not be negligibly small [18].

Chemical bonding in the surface plays a large role in determining the behavior of the plasma-surface interactions. For the case of carbide formation in tungsten, during the annealing of carbon films on tungsten, the carbon begins to strongly react and form carbides with the tungsten substrate at around 900K [20] (although some small amount of carbide exists at the carbon-tungsten interface even at room temperature). Carbide interlayers have also been observed between carbon layers deposited on tungsten substrates when exposed to plasma containing carbon impurities [21]. The chemical erosion properties of a plasma-facing surface that has reacted to form even a partial carbide layer, or when experimentally examining the plasma-interaction behavior of a fully carbidic surface, is completely different from chemical erosion properties of graphite. For a fully carbidized sample the CH_4 production rate drops by at least an order of magnitude compared to that of graphite [22, 23]. Presumably the presence of the carbidic bonding inhibits the production rate of C-H bond formation.

From the modeling perspective, properly including chemical effects becomes even more apparent when the BCA approach to the W/C system is expanded to include the effects associated with large a flux of hydrogen to the system. It is again possible to obtain good agreement between simulation and experimental data [24], but the agreement is obtained after the fact and could not be considered predictive. Determining the appropriate

value to use for the chemical erosion yield of carbon in the ITER situation is particularly difficult given the wide range of measured values in the literature and its dependence on parameters such as temperature [25], flux [26], surface composition [23, 24] and possibly other variables.

A final complication worth mentioning is the possibility, or perhaps even likelihood, of additional elements being present in a confinement device scenario. Exploration of the teriary W/C/O system has shown that the presence of oxygen in a mixed tungsten-carbon surface can inhibit, or in some cases even prevent the formation of tungsten carbide [20]. The presence of oxygen allows for the formation of volatile species, CO and CO_2, which deplete carbon from the surface and influence the amount of carbon available for reaction with surface tungsten. At this stage it is still speculation to attempt to estimate the amount of oxygen that may be present in the ITER vacuum system, although it should be noted that baking in an oxygen atmosphere is being considered as a possible technique to remove tritium-containing codeposits in ITER [27].

An important variable to quantify from a safety perspective is the fuel retention capability of mixed-material plasma-facing surfaces. Again the difficulty becomes how to relate the behavior of plasma-created mixed materials to other measurements. In vacuum annealing measurements of tungsten coated with an amorphous C:H layer, the formation of W_2C is accompanied by a release of hydrogen from the surface [28]. The conclusion drawn is that when a mixed W-C surface forms on a plasma-facing surface it will retain little fuel atoms. However, during deuterium ion beam irradiation studies of a W_2C sample the measured deuterium retention level was between that measured from a clean tungsten surface and a fully carbon covered tungsten surface [29]. Similar measurements obtaining

retention levels of mixed W-C surfaces lying between that of carbon surfaces and tungsten surfaces have also been reported [22, 30, 31].

Beryllium/Carbon System

Material eroded from the ITER first wall will be ionized in the scrape-off layer plasma and tend to flow along the magnetic field toward the divertor. Recent modeling of the transport of eroded material in ITER shows that significant amounts of beryllium may be deposited on the baffle and divertor areas [32].

To first order, the processes used to describe the interaction of carbon ion beams with beryllium samples [33] are similar to the interaction of carbon with tungsten. Initially, the bombardment results in a beryllium carbide rich implantation zone that, due to surface erosion, migrates and eventually become the surface layer. The change in surface layer composition directly effects the composition of material leaving the surface, however, there is a subtle difference between tungsten and beryllium interactions with the incident carbon ions. For the W-C system a primary mechanism responsible for building up carbon layers is the change in the reflection probability for the incident ions due to a lower average mass of the target surface. In the case of the Be-C system, the reflection coefficient does not change appreciably due to the development of the beryllium carbide layer. The effective binding energy calculated by the code changes more dramatically in the Be-C case then in the W-C case and this changes the calculated Be surface loss rate. The TRIDYN code varies the effective surface binding energy linearly between the mean value of the two elemental binding energies and the value of the pure element based on the

composition of the layer [34]. In the case of beryllium, E_b ~ 3.3 eV, and carbon, E_b ~ 7.4 eV, this is a more dramatic effects than between tungsten, E_b ~ 8.9 eV and carbon [35]. Once the surface recession rate is reduced more carbon will build up in the implantation zone and eventually a carbon rich layer results. Calculations based on this mathematical expression for the surface binding energy do a good job of replicating ion beam sputtering results [36, 37]. Similar behavior is predicted for Be ions impinging on a carbon target [38].

While the approximation used to simulate surface binding energies of mixed surfaces appears to work well at higher energy, where the sputtering yield does not vary dramatically with the value for the binding energy, it appears that a more rigorous treatment is needed in the near-threshold-energy range when large amount of deuterium are also present in the surface. The PISCES device has observed the formation of beryllium-rich layers on graphite targets exposed to deuterium plasma containing very small amounts (~0.1%) of beryllium impurities [39, 40]. However, in the inverse Be-C system, namely carbon plasma contamination incident on Be samples, carbon-rich surfaces required a much larger (1-2%) incident impurity fraction to form [41]. While the equilibrium surface composition of the resultant plasma exposed surfaces could be predicted [41, 42] reasonably well using typical values for plasma-material interaction parameters in the literature, the temporal evolution of the surface composition could not be.

The surface of the plasma-exposed samples are observed to evolve over time frames that can be as long as thousands of seconds, or as short as seconds, depending on the plasma experimental conditions [43]. The change in the composition of the surface is correlated to a reduction in the chemical erosion of the graphite sample. As in the case of

tungsten carbide formation in a surface reducing the chemical erosion properties of the bound carbon, beryllium carbide formation in the surface of these samples appears to again be responsible for the reduction [44]. In the plasma environment many parameters can have an influence on the formation of beryllium carbide layers, such as, incident Be flux, surface temperature, incident energy, etc. A systematic variation of plasma and target conditions has resulted in the development of a scaling law to describe the formation time of the beryllium-rich layers in the PISCES experiments [45].

The scaling law is a different approach, compared to using the kinetic Monte Carlo models, to predicting the behavior of mixed-material surfaces. Application of this scaling to typical conditions expected in the ITER divertor provides an estimate of the fluence necessary to inhibit the production of hydrocarbons from the ITER divertor plates. If the extrapolation of this scaling law to ITER is valid, it predicts a beryllium-rich layer to form in approximately 5 milliseconds [45] of ITER-type plasma exposure. This formation time estimate is considerably shorter than the ELM frequency (~1 Hz) expected in ITER, which means that the Be-C mixed-material surfaces may be present most of the time on the ITER divertor plates.

Another issue being addressed in the beryllium-seeded plasma experiments, is the robustness of the beryllium-carbide surfaces to the transient heating effects associated with ELM power losses in ITER. Previous measurements of the existence of thin aluminum layers (as a surrogate for beryllium layers) deposited on graphite and then subjected to extreme power loading revealed that the aluminum did not ablate from the surface until the temperature of the surface exceeded the boiling point of aluminum [46]. While the PISCES-B heat pulsing experiments have not yet achieved a surface temperature

exceeding the boiling temperature of beryllium (T_{boil} = 2744K), or the decomposition temperature of beryllium carbide ($T_{Be2C\ decom.}$ ~ 2400K), they have shown that the protective Be layer forms faster while periodic heat pulses are applied to the samples during the course of the plasma exposure [47]. The quicker suppression of chemical erosion from the plasma-exposed samples is in qualitative agreement with the predictions of the scaling law [45] previously described.

One complication to directly applying these results to predictions for the behavior of ITER is the composition of the incident ion flux to the surface. In measurements involving the tertiary mixed-material Be-C-O system, dramatically different results are obtained. Recall that the interaction of the two-component Be-C system resulted in the formation of a Be_2C layer, the bombardment of beryllium with CO^+ ion beams results in almost exclusive binding of the beryllium to the oxygen in the implantation zone [33, 37]. The carbon atoms present are then bound up in C-C or C-O bonds. Once this implantation zone reaches the receding surface, the carbon is easily chemically eroded. The differences between these measurements and those described in the PISCES simulator relate to the amount of oxygen present in the incident ion flux. Depending on the level of oxygen present in ITER, the final behavior may lie somewhere between the two results described.

A trend similar to that observed with the W-C system with respect to hydrogen release is also exhibited during formation of beryllium carbide obtained by reacting a surface layer of amorphous C:H with a beryllium substrate. Once the carbide reaction begins to occur, typically in the temperature range of 773K to 873K, hydrogen is released from the reacted material [48, 49]. Again, such a result does not guarantee that Be_2C bombarded with energetic hydrogen isotopes will retain little of the incident particle

fluence. Deuterium ion beam implantation into mixed Be-C layers showed higher retention in the mixed-material samples, compared to clean Be samples [50]. Retention measurements from plasma created mixed-material targets also show larger retention in mixed Be-C layers compared to clean Be targets [41], but surprisingly mixed Be-C targets also show larger retention when compared with clean carbon targets exposed to identical plasma discharges [44]. In both cases of plasma-created mixed Be-C (Be incident on C and C incident on Be) surfaces the differences in retention are largest during low surface temperature exposure. The differences in retention decrease as the exposure temperature increases.

For the ITER device, the dominant term driving the tritium inventory in the vessel is predicted to be codeposition of tritium with eroded material, rather than implantation and retention in plasma exposed target surfaces [27]. The eroded material capable of codepositing will be determined by the mixed-material surfaces with which the plasma interacts. In measurements of codeposition of deuterium with a mixed Be-C-O layer [51], the deuterium concentration was observed to be similar to that of codeposition of deuterium with pure carbon. The hypothesis was that deuterium was coimplanting into a growing BeO film, rather than codepositing with the smaller amount of carbon present in the films. Subsequent measurement seemed to confirm this hypothesis, as the measured deuterium content in coimplanted Be films seemed to scale with the cleanliness of the films produced [52]. During PISCES beryllium seeded plasma experiments when Be_2C surface layers form on mixed-material targets, the codepositing material is measured to consist almost exclusively of beryllium [53] with a varying amount of oxygen present in the coimplanted beryllium. However, during the PISCES codeposited material collection,

films collected at higher temperature had decreasing amounts of deuterium retained in the films, yet also contained an increasing amount of oxygen. It has been suggested that the varying concentration of deuterium is governed by the energy of the incident deuterium during the coimplantation rather than by the oxygen content in the films [54].

While the mechanism governing the retention is still under investigation, certain information is already clear. First, if beryllium-rich layers form on ITER plasma-facing materials, then the codepositing material will consist primarily of beryllium. Second, although the level of codeposition, or coimplantation, in beryllium-rich layers at room temperature is similar to that expected in carbon-rich codeposits, the concentration decreases much more rapidly with temperature in beryllium codeposits than it does in carbon codeposits. And finally, it appears to be easier to remove the deuterium content in beryllium-rich codeposits at lower temperature than from carbon-rich codeposits. This last fact is shown in Figure 1, where data from outgassing measurements of beryllium-rich codeposits [53] is replotted and compared to data from thermally desorbing carbon-rich codeposits [55]. Also indicated in the figure is the design value for the maximum bake temperature achievable in the ITER divertor (650K) after the coolant is drained from the divertor components.

Beryllium/Tungsten System

The third binary system of materials that is a concern for the ITER design is that of beryllium-tungsten alloys, so called tungsten beryllides. While the existence of these alloys (Be_2W, $Be_{12}W$ and $Be_{22}W$) has been known for some time [56], it is only recently that

their importance has been recognized. The primary reason for concern stems from the beryllium plasma-seeding experiments carried out in the PISCES Laboratory. In the initial series of measurements the beryllium-supplying oven contained a tungsten crucible holding the molten beryllium. This crucible melted and destroyed the oven while operating at only about 1500K [57]. The uncertainty associated with any possibility for a similar major malfunction in the ITER divertor region has brought significant new effort to this area. A detailed description of tungsten beryllides is presented in these proceedings [58] and so will not be repeated here.

The formation of beryllides will be governed by the conditions experienced by tungsten plasma-facing materials due to interaction with the incident plasma. Since the temperature of the surface must be fairly large (~1100K or more) to allow significant growth of the alloy, the loss rate of beryllium from these surfaces will be impacted significantly by both thermal sublimation and thermally enhanced erosion of beryllium [59] from the material. A model has been proposed to describe plasma conditions that should result in the formation of a beryllium layer on a plasma exposed tungsten surface [60] and this model should provide insight into which surfaces in ITER might be most susceptible to beryllide formation.

While there is presently no data available concerning retention, or codeposition, of deuterium in Be/W alloys, one might expect that when and if these alloys form, the codeposited material will consist primarily of beryllium and the codeposition discussion presented in the previous section will hold. In addition there has been little, if any, codeposition of deuterium with tungsten observed experimentally [61].

A final word of caution is perhaps in order with regard to similar consequences from unexpected mixed-material formation. There has been an ongoing discussion in the community about the necessity of designing a boronization system for possible use in ITER. Similar to the tungsten-beryllide alloys, tungsten-boride alloys exist [62] that have melting temperatures lower than that of elemental tungsten. In addition, beryllium-boride alloys could form on the beryllium first wall. The beryllium boride phase diagram, Figure 2, shows that the mixed Be-B system can even have a melting temperature lower than that of elemental beryllium [63].

Summary

Due to the combination of materials employed in different locations in the ITER design there is a strong likelihood that some types of mixed materials will form on plasma-facing surfaces. This review has summarized present knowledge of each of the three binary mixed-material systems, C/W, Be/C and Be/W. The added complications associated with including the effects of oxygen, or hydrogen, in the mix have also been discussed. While no definitive conclusions can yet be drawn concerning the implication of mixed materials in ITER, there have been significant advancements in the understanding of mixed materials in recent years.

The ability of models to correctly predict the formation conditions of mixed materials depends critically on chemical effects in the surface layers. Unfortunately, the inclusion of chemistry in kinetic models must be done in some ad hoc manner based on literature values that may not be applicable to plasma-created mixed materials. Likewise

the large fluence of particles associated with plasma facing surfaces in ITER may not be compatible with a molecular dynamics modeling approach to the mixed systems. Some technique is urgently needed to self-consistently address the issue of chemical effects with respect to plasma-surface interactions.

It is clear that the mixing of materials in plasma-facing surfaces can alter the hydrogenic retention properties of surfaces. In the W/C case, the retention level seems to lie between those expected from the pure materials. In the Be/C case, retention is increased somewhat above that expected from pure carbon. However, the largest impact on the tritium accumulation inside the ITER vessel appears to be associated with changes in the hydrogenic inventory in codeposited layers located in regions away from direct plasma contact. The composition of codeposited layers, and thereby their hydrogen retention properties, may be determined by the erosion properties of mixed materials, as has been seen in the PISCES experiments. Or the codeposited materials containing W/C or Be/C mixes may react similar to laboratory carbide formation measurements that observe the release of hydrogen when carbides form. Finally, the retention properties of the tungsten beryllides is still completely unknown and it can only be hoped that the elevated temperature required for their formation may mitigate any adverse effects.

Acknowledgements

It is my pleasure to acknowledge many useful discussions with, and suggestions from, the members of the PISCES Laboratory and our European collaborators. In particular, I would

like to thank Prof. Marie Doerner for her editing and, Dr. Matthew Baldwin and Prof. Sergei Krasheninnikov, for their input.

References

[1] ITER Technical Basis, ITER EDA Documentation Series No. 24, IAEA, Vienna, 2002.
[2] S. A. Cohen et al., J. Nucl. Mater. 76&77 (1978) 459.
[3] B. E. Mills et al., J. Nucl. Mater 162-164(1989)343.
[4] M. Rubel et al., J. Nucl. Mater. 313-316(2003)321.
[5] J. Likonen, E. Vainonen-Ahlgren, J. P. Coad et al., J. Nucl. Mater. 337-339(2005)60.
[6] J. P. Coad, P. L. Andrew and A. T. Peacock, Phys. Scripta T81(1999)7.
[7] J. P. Coad, P. Andrew, D. E. Hole et al., J. Nucl. Mater. 313-316(2003)419.
[8] G. F. Matthews, J. Nucl. Mater. 337-339(2005)1.
[9] B. A. Carreras, J. Nucl. Mater. 337-339(2005)315.
[10] S. J. Zweben and R. W. Gould, Nucl. Fusion 25(1985)171.
[11] A. Loarte, G. Saibene, R. Satori et al., Phys. Plasmas 11,5(2004)2668.
[12] W. Eckstein and J. Roth, Nucl. Instr. & Methods in Phys.Res. B53(1991)279.
[13] W. Moeller, W. Eckstein and J. P. Biersack, Comp. Phys.Commun. 51(1988)355.
[14] R. Kawakami and K. Ohya, Jpn. J. Appl. Phys. 40(2001)5399.
[15] W. Eckstein, C. Garcia-Rosales, J. Roth and W. Ottenberger, Sputtering Datt IPP Report 9/82(1993).
[16] W. Eckstein, V. I. Shulga nd J. Roth, Nucl. Instr. & Methods in Phys.Res. B153(1999)415.
[17] R. Kawakami and K. Ohya, Jpn. J. Appl. Phys. 42(2003)5259.
[18] K. Schmid and J. Roth, J. Nucl. Mater. 302(2002)96.
[19] Ch. Linsmeier, J. Luthin and P. Goldstrass, J. Nucl. Mater. 290-293(2001)25.
[20] J. Luthin and Ch. Linsmeier, J. Nucl. Mater. 290-293(2001)121.
[21] F. C. Sze, L. Chousal, R. P. Doerner et al., J. Nucl. Mater. 266-269(1999)1212.
[22] W. Wang, V. Kh. Alimov, B. M. U. Scherzer et al., J. Nulc. Mater. 241-243(1997)1087.
[23] M Taniguchi, K. Sato, K. Ezato et al., J. Nucl. Mater. 313-316(2003)360.
[24] K. Schmid and J. Roth, J. Nucl. Mater. 313-316(2003)302.
[25] J. W. Davis and A. A. Haasz, J. Nucl. Mater. 241-243(1997)37.
[26] J. Roth, R. Preuss, W. Bohmeyer et al., Nucl. Fusion 44(2004)L21.
[27] G. Federici, R. A. Anderl, P. Andrew et al., J. Nucl. Mater 266-269(1999)14.
[28] K. Ashida, K. Fujino, T. Okabe et al., J. Nucl. Mater. 290-293(2001)42.
[29] R. A. Anderl, R. J. Pawelko and S. T. Schuetz, J. Nucl. Mater. 290-293(2001)38.
[30] V. Kh. Alimov, Phys. Scripta, T108(2004)46.
[31] O. V. Ogorodnikova, J. Roth and M. Mayer, J. Nucl. Mater. 313-316(2003)469.
[32] J. N. Brooks et al., these proceedings.
[33] P. Goldstrass and Ch. Linsmeier, J. Nucl. Mater. 290-293(2001)71.
[34] W. Eckstein, M. Hou and V. I. Shulga, Nucl. Instrum. & Meth. In Phys. Res. B 119(1996)477.
[35] C. Kittel, Introduction to Solid State Physics (Wiley, New York, 1976).
[36] E. Gauthier, W. Eckstein, J. Laszlo et al., J. Nucl. Mater. 176&177(1990)438.
[37] P. Goldstrass, W. Eckstein and Ch. Linsmeier, J. Nucl. Mater. 266-269(1999)581.
[38] W. Eckstein, J. Nucl. Mater. 281(2000)195.
[39] R. P. Doerner, M. J. Baldwin and K. Schmid, Phys. Scripta T111(2004)75.
[40] K. Schmid, M. Baldwin, R. Doerner and A. Wiltner, Nucl Fusion 44(2004)815.

[41] R. P. Doerner, A. A Grossman, S. C. Luckhardt et al., J. Nucl. Mater. 266-269(1999)392.
[42] K. Schmid, M. Baldwin and R. Doerner, J. Appl. Phys. 97(2005)064912.
[43] M. J. Baldwin and R. P. Doerner, Nucl. Fusion 46(2006)444.
[44] M. J. Baldwin, R. P. Doerner, K. Schmid et al., submitted to J. Nucl. Mater. (2006).
[45] D. Nishijima et al., these proceedings.
[46] G. Federici, A. Zhitlukhin, N. Arkhipov et al., J. Nucl. Mater. 337-339(2005)684.
[47] R. Pugno et al., these proceedings.
[48] K. Ashida, K. Watanabe and T. Okabe, J. Nucl. Mater. 241-243(1997)1060.
[49] J. Roth, W. R. Wampler and W. Jacob, J. Nucl. Mater. 250(1997)23.
[50] R. A. Anderl, G. R. Longhurst, R. J. Pawelko et al., J. Fusion Energy 16(1997)95.
[51] M. Mayer, J. Nucl. Mater. 240(1997)164.
[52] R. A. Causey and D. S. Walsh, J. Nucl. Mater. 254(1998)84.
[53] M. J. Baldwin, K. Schmid, R. P. Doerner et al., J. Nucl. Mater. 337-339(2005)590.
[54] A. V. Markin, V. P. Dubkov, A. E. Gorodetsky et al., J. Nucl. Mater. 283-287(2000)1094.
[55] R. A. Causey, W. R. Wampler and D. S. Walsh, J. Nucl. Mater. 176&177(1990)992.
[56] C. R. Watts, Int. J. Powder Met. 4(1968)49.
[57] R. P. Doerner, M. J. Baldwin and R. A. Causey, J. Nucl. Mater. 342(2005)63.
[58] Ch. Linsmeier, these proceedings.
[59] R. P. Doerner, S. I. Krasheninnikov and K. Schmid, J. Appl. Phys. 95(2004)4471.
[60] M. J. Baldwin, these proceedings.
[61] M. Mayer, R. Berisch, H. Plank et al., J. Nucl. Mater. 230(1996)67.
[62] H. Itoh, T. Matsudaira, S. Naka et al., J. Mater. Sci. 22(1987)2811.
[63] T. Massalski (Ed.), Binary Alloy Phase Diagrams, ASM International, Metals Park, OH, 1987, p. 341.

Figure Captions

Figure 1 – Comparison of hydrogen isotope desorption characteristics from beryllium based and carbon based codeposits.

Figure 2 – Phase diagram of beryllium boride [61].

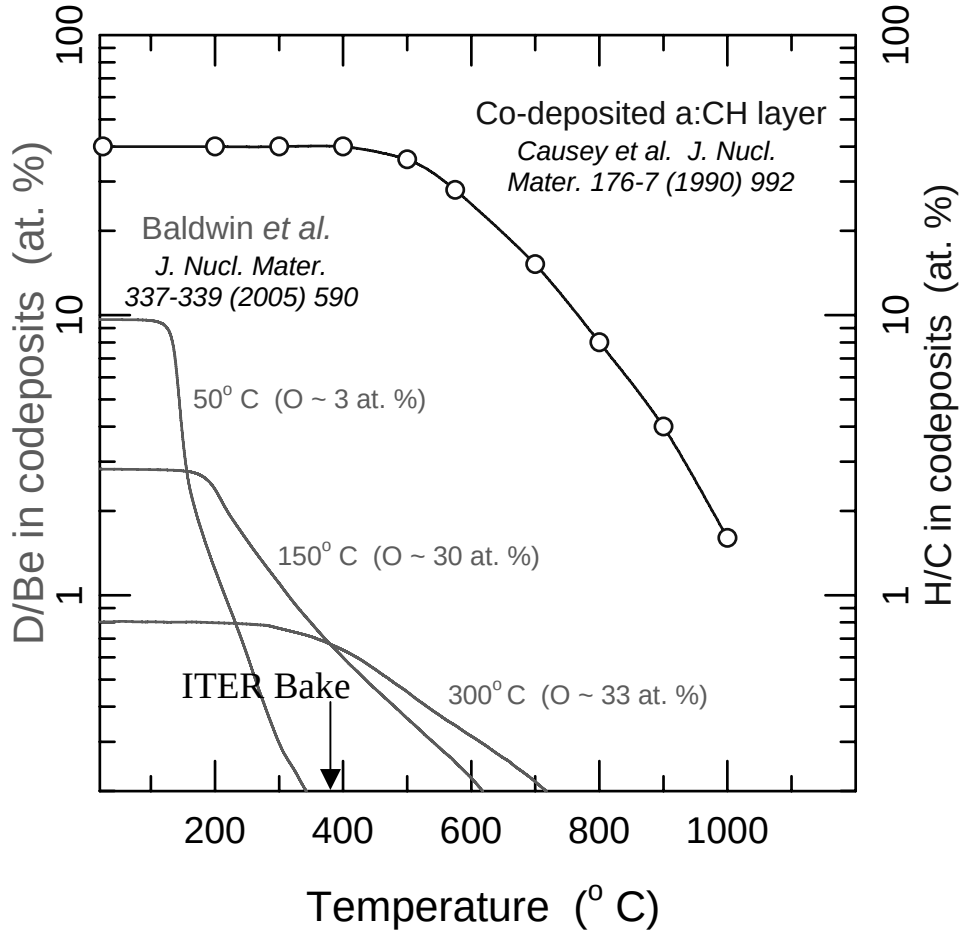
D/Be in codeposits (at. %)
H/C in codeposits (at. %)
100
10
1
Co-deposited a:CH layer
Causey et al. J. Nucl. Mater. 176-7 (1990) 992
Baldwin et al.
J. Nucl. Mater. 337-339 (2005) 590
50° C (O ~ 3 at. %)
150° C (O ~ 30 at. %)
300° C (O ~ 33 at. %)
ITER Bake
200
400
600
800
1000
Temperature (° C)

Figure 1

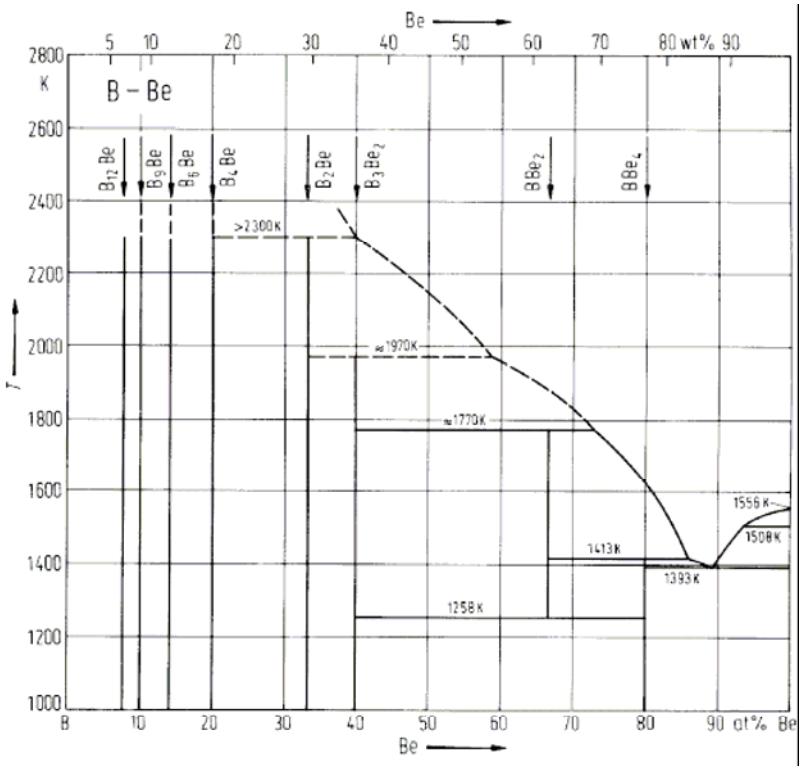
B – Be
Be
5 10 20 30 40 50 60 70 80 wt% 90
2800 K
2600
2400
2200
2000
1800
1600
1400
1200
1000
T
B12Be
B9Be
B6Be
B4Be
B2Be
B3Be2
BBe2
BBe4
≈2300K
≈1970K
≈1770K
1556K
1508K
1413K
1393K
1258K
B 10 20 30 40 50 60 70 80 90 at% Be
Be

Figure 2

P2-53

Parametric studies of carbon erosion mitigation dynamics in beryllium seeded deuterium plasmas

D. Nishijima*, M.J. Baldwin, R.P. Doerner and R. Seraydarian

Center for Energy Research, University of California at San Diego,

9500 Gilman Dr., La Jolla, CA 92093-0417, USA

Abstract

The characteristic time of protective beryllium layer formation on a graphite target, $\tau_{Be/C}$, has been investigated as a function of surface temperature, T_s, ion energy, E_i, ion flux, Γ_i, and beryllium ion concentration, c_{Be}, in beryllium seeded deuterium plasma. $\tau_{Be/C}$ is found to be strongly decreased with increasing T_s in the range of 550-970 K. This is thought to be associated with the more efficient formation of beryllium carbide (Be_2C). By scanning the parameters, a scaling expression for $\tau_{Be/C}$ has been derived as,

$\tau_{Be/C}$ [s] = $1.0\text{x}10^{-7}\ c_{Be}^{-1.9\pm0.1}\ E_i^{0.9\pm0.3}\ \Gamma_i^{-0.6\pm0.3}\ \exp((4.8\pm0.5)\text{x}10^3/T_s)$.

Should this scaling extend to an ITER scenario, carbon erosion of the divertor strike point region may be reduced with characteristic time of ~ 6 ms. This is much shorter than the time between predicted ITER type I ELMs (~ 1 s), and suggests that protective beryllium layers can be formed in between ELMs, and mitigate carbon erosion.

PACS: 52.40.Hf

JNM Keywords: Beryllium, Beryllium Alloys and Compounds, Carbon, Divertor Materials, Plasma-Materials Interaction

PSI-17 Keywords: PISCES-B, Beryllium, Carbon, Mixed-material, Chemical erosion

**Corresponding author address:* Center for Energy Research, University of California at San Diego, 9500 Gilman Dr. Mail Code: 0417, La Jolla, CA 92093, USA

**Corresponding author e-mail:* dnishijima@ferp.ucsd.edu

Presenting author: Daisuke Nishijima

Presenting author e-mail: dnishijima@ferp.ucsd.edu

1. Introduction

Mixed-material effects have attracted great interest since ITER will have beryllium, carbon and tungsten as plasma facing components (PFCs). Beryllium sputtered from the first wall is expected to migrate to the divertor region, where the strike point region is made of carbon material. Tungsten is used in the baffle region. Since the beryllium concentration in the divertor plasma is predicted to be in the range of 0.01-0.1, interaction of beryllium with carbon and tungsten materials may change the original properties of those materials.

Previous experiments [1, 2] on beryllium/carbon mixed-material effects in the linear divertor plasma simulator PISCES-B revealed that both chemical and physical erosion of carbon was mitigated by beryllium impurities in the plasma. This was identified by a reduction of CD ($A^2\Delta$-$X^2\Pi$) band intensity and C I line intensity. X-ray photoelectron spectroscopy (XPS) analyses of these targets subsequent to plasma exposure revealed the formation of beryllium carbide (Be_2C), which is thought to play an important role in carbon erosion mitigation. Work on beryllium/tungsten mixed-material effects has been also performed in PISCES-B, and is reported in these proceedings [3].

In this paper we extend previous work [2] on carbon erosion mitigation in beryllium seeded deuterium plasma. In ref. [2], the dependence of the protective beryllium layer formation time, $\tau_{Be/C}$, on beryllium ion concentration, c_{Be}, was investigated. Here, we reveal further dependence of $\tau_{Be/C}$ on other parameters, such as incident ion energy, E_i, surface temperature, T_s, and incident ion flux, Γ_i. A scaling law for $\tau_{Be/C}$ is derived from a regression analysis of the data and this scaling is used to predict carbon erosion behavior under ITER divertor relevant

conditions.

2. Experimental setup

Experiments are performed in the linear divertor plasma simulator PISCES-B [4], which produces a high flux (up to 10^{23} $m^{-2}s^{-1}$) steady state plasma. ATJ graphite targets, 22 mm in diameter and 2.8 mm thick, are exposed to beryllium seeded deuterium plasmas. Beryllium impurities are injected into the plasma column using a high-temperature effusion cell (Veeco Applied EPI), located at ~ 150 mm upstream from the target as shown in figure 1. The amount of beryllium impurities can be controlled by varying the temperature of effusion cell. The injected beryllium atoms are ionized in the plasma and transported to the target. The singly ionized beryllium density, n_{Be+}, in the plasma is obtained from Be II (λ = 467.3 nm) line intensity measured with an absolutely calibrated spectroscopic system. The necessary photon emission coefficient is taken from the ADAS database [5]. The electron density, n_e, the electron temperature, T_e, and the ion flux, Γ_i, are measured with a fast scanning double probe system at the same axial position as the effusion cell. The incident ion energy, E_i, is controlled by biasing the target with a negative potential relative to the plasma potential. The sample temperature is measured with a thermocouple contacted to the back side of target.

3. Measuring $\tau_{Be/C}$

The characteristic time of protective beryllium layer formation on a graphite sample, in other words, the carbon erosion mitigation time, $\tau_{Be/C}$, is determined from the decay of CD ($A^2\Delta$-

$X^2\Pi$) band intensity around $\lambda \sim 430$ nm as shown in figure 2. In ref. [2], the CD band intensity decay is found to correlate closely with beryllium layer formation on a graphite sample. At $t = 0$ s, beryllium is injected into the plasma by opening the shutter of the effusion cell. During the exposure, the D_γ intensity is fairly constant, indicating that the plasma conditions are unchanged. The subtraction of CD band intensity taken in a region far from the target (~ 70 mm upstream) is used to eliminate the effects of the intensity originating from wall carbon erosion [2, 6]. From the exponential fit, $\tau_{Be/C}$ is derived in this example to be around 83 s.

4. Individual parameter dependence of $\tau_{Be/C}$

In figure 3, $\tau_{Be/C}$ is plotted as a function of beryllium ion concentration, $c_{Be} = n_{Be+}/n_e$. In this data set, E_i, T_s and Γ_i are kept constant for three different plasma regimes. As reported in ref. [2], the higher c_{Be} leads to the shorter $\tau_{Be/C}$, where a power function fit, $\tau_{Be/C} = \alpha\, c_{Be}^{\beta}$, gives $\beta \sim -2$. The additional data confirm the c_{Be} dependence of $\tau_{Be/C}$ at different Γ_i and T_s that were not investigated in ref. [2].

Figure 4 shows the dependence of $\tau_{Be/C}$ on E_i for the chosen value of $c_{Be} = 10^{-3}$ by assuming $\beta = -2$ in the power law, $\tau_{Be/C} = \alpha\, c_{Be}^{\beta}$ to compensate the c_{Be} dependence. The dependence on T_s and Γ_i is not compensated. It is found from figure 4 that $\tau_{Be/C}$ increases with E_i, at least up to ~ 85 eV. This tendency can be qualitatively explained by the fact that beryllium deposited on the graphite target can be more readily sputtered at higher E_i, thus resulting in a longer $\tau_{Be/C}$.

As shown in figure 5, where $\tau_{Be/C}$ is similarly calculated at $c_{Be} = 10^{-3}$ with $\beta = -2$ from measured

data, $\tau_{Be/C}$ is found to strongly depend on T_s. At a higher T_s of ~ 950 K ($1/T_s$ ~ 0.001 K^{-1}), $\tau_{Be/C}$ is shorter than that at T_s ~ 600 K ($1/T_s$ ~ 0.0017 K^{-1}) by a factor of ~ 20. This observation is qualitatively consistent with XPS analyses of graphite samples exposed to beryllium seeded deuterium plasmas at several different T_s [7]. Namely, the higher T_s leads to increased reaction of the beryllium and carbon, resulting in full surface carbidisation with Be_2C.

An Arrhenius exponential function is used to fit the surface temperature dependent data since a surface reaction rate, K, is generally described by an exponent of a ratio of the enthalpy of formation, ΔH_{298}, to T_s. The enthalpy of formation of Be_2C, $\Delta H_{298}(Be_2C)$, is reported as –117.0±1.0 kJ/mol [8], giving the Be_2C formation time as, $\tau_{Be2C} \propto 1/K_{Be2C} \propto \exp(1.4e4/T_s)$. The numerator in the exponential function is around 3 times larger than that in the protective beryllium layer formation time, $\tau_{Be/C} \propto \exp(4.6e3/T_s)$, derived from the experiments, meaning that $\tau_{Be/C}$ has the weaker T_s dependence than τ_{Be2C}. This implies that pure beryllium layers on Be_2C also contributes to the carbon erosion reduction especially at lower T_s and/or $\Delta H_{298}(Be_2C)$ may be lower in the plasma-material interaction environment than the equilibrium value reported in the literature. It should be noted that our value is very similar to around 5000 K obtained from an Arrhenius plot of the intensity of $Be_2C(111)$ peak measured with X-ray diffractometry (XRD), where a carbon film was deposited on a beryllium plate by rf discharge of C_2H_4, subsequently the sample was heated up at given temperatures [9].

5. Scaling expression for $\tau_{Be/C}$ and extrapolation to ITER condition

Given the experimentally determined parametric forms, a regression analysis was performed with

the parameters, c_{Be}, E_i, T_s and Γ_i to obtain a scaling law for $\tau_{Be/C}$. In figure 6 the experimentally derived $\tau_{Be/C}$ is compared with the scaling expression,

$$\tau_{Be/C}^{scale}\ [s] = 1.0\text{x}10^{-7}\ c_{Be}^{-1.9\pm0.1}\ E_i^{0.9\pm0.3}\ \Gamma_i^{-0.6\pm0.3}\ \exp((4.8\pm0.5)\text{x}10^3/T_s), \quad (1)$$

where $c_{Be} = n_{Be+}/n_e$ is dimensionless, E_i in eV, Γ_i in 10^{22} $m^{-2}s^{-1}$ and T_s in K. Each parameter scan range is shown in the figure. The experimental values are found to agree well with the scaling law. Note that the exponent of each parameter is slightly different from that shown in the previous section since in the individual parameter scan (Figures 3, 4 and 5) the dependence on other parameters are not precisely taken into account while the c_{Be} dependence is compensated by using $\beta = -2$.

It is found from the scaling law that $\tau_{Be/C}$ has a negative power law dependence on Γ_i. This is because a larger fraction of sputtered beryllium atoms from the target is ionized in the plasma at higher fluxes, therefore the redeposited fraction of beryllium is increased, contributing to quicker beryllium layer formation.

Although some of typical values for the parameters expected in the ITER divertor carbon targets are outside our scanned ranges, the scaling law can be used to predict the protective beryllium layer formation time in the ITER situation. With $c_{Be} = 0.05$, $E_i = 20$ eV, $T_s = 1200$ K and $\Gamma_i = 10^{23}$ $m^{-2}s^{-1}$ [10], the scaling expression gives $\tau_{Be/C} \sim 6$ ms, which is much shorter than a predicted ITER type I ELM period, i.e. the inverse of ELM frequency, of ~ 1 s [11]. This suggests that protective beryllium layers on carbon targets can be formed in between ELMs, thereby reducing the carbon erosion during the period between ELMs.

6. Conclusion

We have derived a scaling expression for the characteristic formation time of protective beryllium layer on a graphite sample from parametric scan experiments in beryllium seeded deuterium plasmas of the PISCES-B linear divertor simulator. The scaling expression is in good agreement with the experimentally derived beryllium layer formation time. The predicted formation time in a typical ITER divertor condition is found to be much shorter than the inverse of expected ITER type I ELM frequency of ~ 1 Hz. This result is favorable for mitigating carbon erosion. We plan to extend the experimental parameter ranges to increase confidence in the scaling law.

Acknowledgements

The authors express their sincere thanks to PISCES technical staff for their professional skill and dedication. Discussion with PISCES scientific members was really fruitful. This work is conducted under the US Department of Energy Contract: DOE DE-FG03-95ER-54301.

References

[1] R.P. Doerner et al., *Proc. 20th IAEA Fus. Ener. Conf. (Vilamoura, Portugal, 2004),* IT/P3-18.

[2] M.J. Baldwin and R.P. Doerner, Nucl. Fusion **46** (2006) 444.

[3] M.J. Baldwin et al., in these proceedings.

[4] R.P. Doerner et al., Physica Scripta. **T111** (2004) 75.

[5] H.P. Summers, Atomic Data and Analysis Structure-User Manual, Report JET-IR(94), JET Joint Undertaking, Abingdon (1994).

[6] D.G. Whyte et al., Nucl. Fusion **41** (2001) 47.

[7] M.J. Baldwin et al., submitted to J. Nucl. Mater.

[8] O. Kubaschewski et al., Materials Thermo-chemistry, 6th Ed., Pegamon Press, Oxford 1993.

[9] K. Ashida et al., J. Nucl. Mater. **241-243** (1997) 1060.

[10] G. Federici et al., J. Nucl. Mater. **266-269** (1999) 14.

[11] G. Federici et al., Plasma Phys. Control. Fusion **45** (2003) 1523.

Figure captions

Figure 1. Schematic view of the target region in the linear divertor plasma simulator PISCES-B. A graphite target is exposed to a beryllium seeded deuterium plasma.

Figure 2. Time evolution of D_γ, normalized Be I (457.3 nm) and CD ($A^2\Delta$-$X^2\Pi$) band intensity near the target during a beryllium seeded deuterium plasma exposure of a graphite target (c_{Be} ~ 1.3x10^{-3}, T_s ~ 800 K, E_i ~ 34 eV, Γ_i ~ 3.5x10^{22} $m^{-2}s^{-1}$). The CD band intensity taken in a region far from the target is subtracted from that near the target to eliminate changes in the CD band intensity originating from wall carbon erosion.

Figure 3. Beryllium ion concentration, c_{Be}, dependence of $\tau_{Be/C}$ at three different conditions with E_i of ~ 40 eV. Circles: Γ_i ~ 1x10^{22} $m^{-2}s^{-1}$, T_s ~ 690±10 K, Squares: Γ_i ~ 3x10^{22} $m^{-2}s^{-1}$, T_s ~ 600±50 K [2], Diamonds: Γ_i ~ 3x10^{22} $m^{-2}s^{-1}$, T_s ~ 955±20 K. Lines show results of power function fits ($\tau_{Be/C} = \alpha\, c_{Be}^{\beta}$), revealing β ~ -2.

Figure 4. Incident ion energy, E_i, dependence of $\tau_{Be/C}$. To compensate the c_{Be} dependence, $\tau_{Be/C}$ is calculated at $c_{Be} = 10^{-3}$ with $\beta = -2$ in the power law, $\tau_{Be/C} = \alpha\, c_{Be}^{\beta}$, from measured data.

Figure 5. Surface temperature, T_s, dependence of $\tau_{Be/C}$. Similarly, $\tau_{Be/C}$ is derived at $c_{Be} = 10^{-3}$ with $\beta = -2$ from measured data.

Figure 6. Comparison of experimental protective beryllium layer formation time, $\tau_{Be/C}^{exp}$, with the scaling expression in eq. (1).

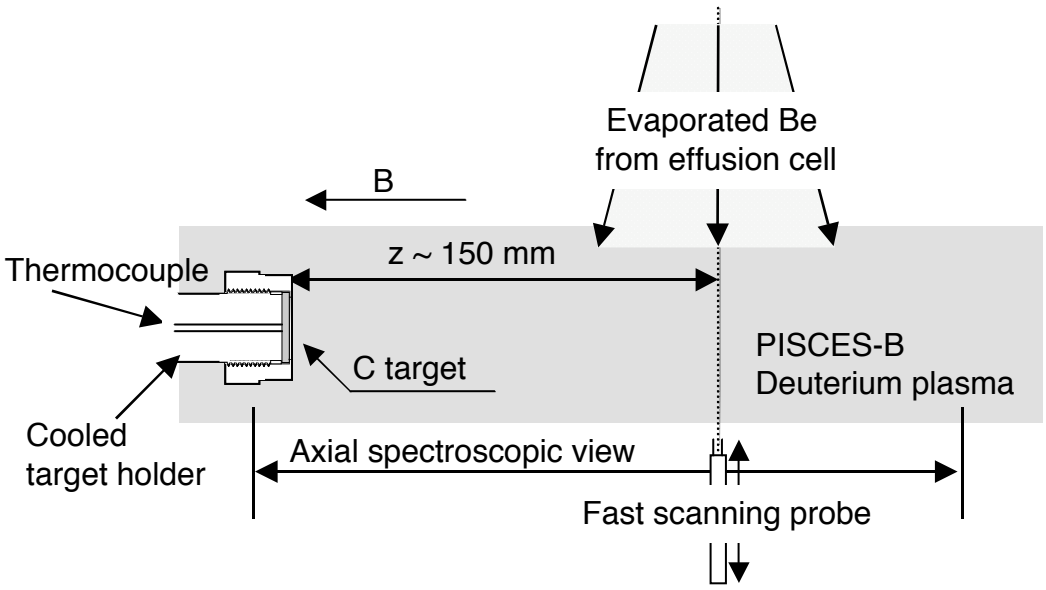

Figure 1. D. Nishijima et al

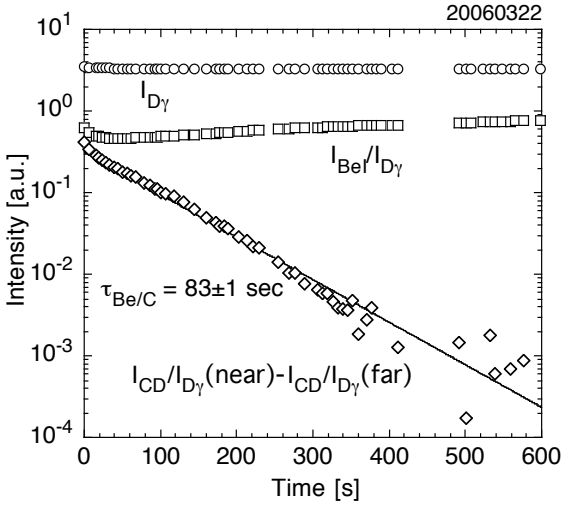

Figure 2. D. Nishijima et al

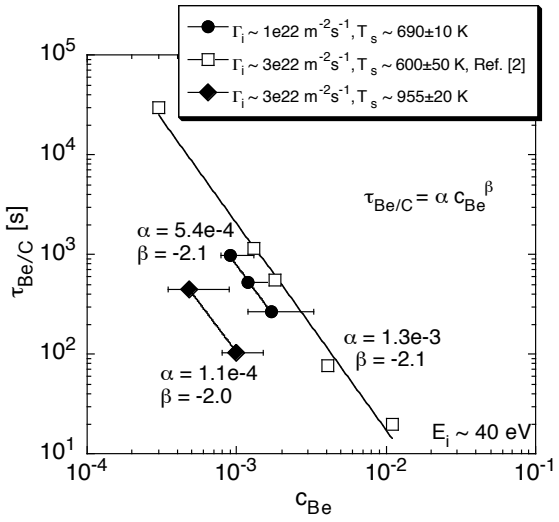

Figure 3. D. Nishijima et al

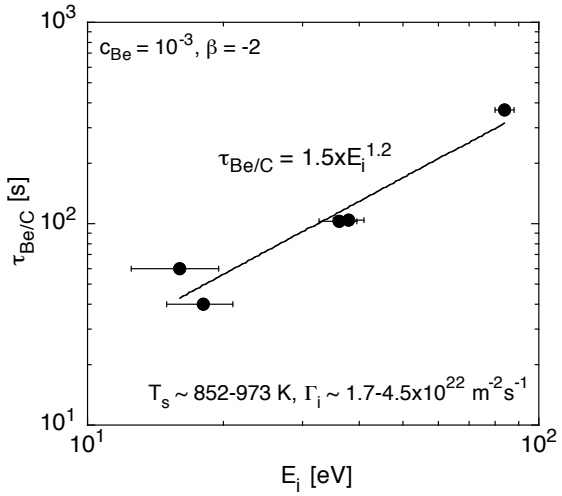

Figure 4. D. Nishijima et al

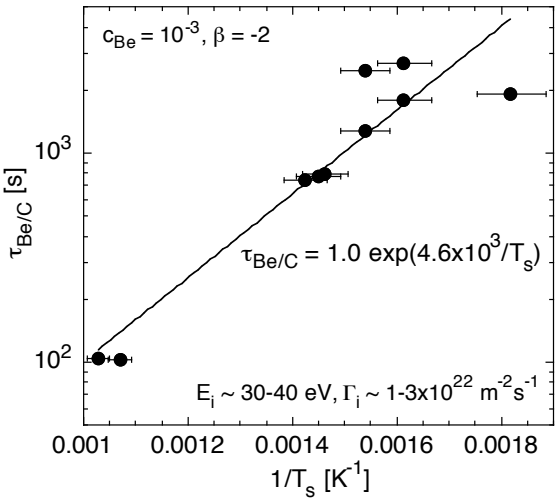

Figure 5. D. Nishijima et al

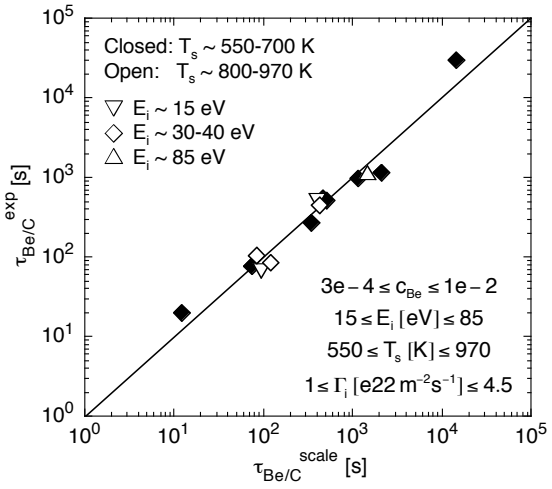

Figure 6. D. Nishijima et al

P3-43

Examination of the velocity time-delay-estimation technique

J. H. Yu*, C. Holland, G. R. Tynan, G. Antar, Z. Yan

University of California, San Diego, La Jolla, CA 92093, USA

Abstract

The one-dimensional time-delay-estimation (TDE) velocity technique infers the velocity of plasma fluctuations using cross-correlations between two spatially separated signals, and here this technique is evaluated using experimental results and numerical simulations. Probe arrays and a fast-framing imaging camera are used to measure the azimuthal fluctuation propagation speed in a cylindrical magnetized plasma device. The time-averaged TDE velocity field obtained in this way is found to be approximately 30% larger than Mach probe measurements of the plasma fluid velocity, suggesting that the TDE method infers the plasma *ExB* velocity and presumably a diamagnetic flow. The TDE technique is also applied to turbulent simulation data with known velocity fields. The results show that one-dimensional TDE techniques can be used to infer the large-scale, slowly varying velocity, but that small scale or turbulent velocity fields cannot be reliably inferred with such one-dimensional approaches.

PACS: 52.30.-q, 52.35.Ra, 52.35.Kt
JNM keywords: Diffusion, Experimental Techniques
PSI-17 keywords: Cross-Field Transport, Edge Plasma, Fluctuations and turbulence, Plasma flow
**Corresponding author address*: 9500 Gilman Dr., MC 0417, La Jolla, CA 92093, USA
**Corresponding author E-mail*: jyu@ferp.ucsd.edu
Presenting author: Jonathan H. Yu
Presenting author e-mail: jyu@ferp.ucsd.edu

INTRODUCTION

Measurements of both the time-averaged and turbulent plasma velocity fields are desirable to validate theories and simulations of edge plasma turbulence, edge plasma flows, material migration, and plasma surface interactions. Several schemes for inferring the plasma velocity field from time-resolved imaging diagnostics have recently been proposed [1,2,3]. The simplest of these schemes is based on the cross-correlation analysis of two spatially-separated fluctuation measurements, and we denote this technique as the velocity time-delay estimation (TDE).

The TDE method has a rich history in neutral fluids [4]. In recent work the TDE method is applied to density fluctuation measurements obtained with beam emission spectroscopy [5], showing the existence of geodesic acoustic modes [6] (GAMs), which are finite frequency zonal flows [7] and are believed to be a major player in edge turbulence in DIII-D and other machines such as ASDEX Upgrade, JFT-2M, and the CHS stellarator. The TDE technique is being pursued as a way to infer the turbulent velocity associated with turbulent fluxes at locations inside the separatrix [8,9]. Caution should be used, however, when applying the results of the TDE algorithm to quantify the actual advection of particles (which is due only to guiding center drifts such as *ExB* flow). The fluctuations generally cannot be treated as passive tracers in a background advecting flow, because diamagnetic effects can drive a phase velocity relative to the mean plasma flow.

In this paper, we focus on steady flows in the experiments, and compare the 1D TDE scheme applied to probes and imaging data. Both the probes and the fast-framing imaging yield similar TDE velocity profiles, opening the possibility of using images to infer the velocity field in regions where probes cannot be used. The TDE measurement is then compared to Mach

probe measurements of the ion fluid velocity. We use simulations to further understand how the TDE technique relates to *ExB* drifts and diamagnetic effects.

TDE METHOD

Fluctuations (density, potential, or image intensity) are sampled at rate $1/\Delta t$, and the time lag τ_p is calculated between the two spatially-separated signals based on the peak of the cross correlation $R_{\Delta x}(\tau) = \frac{1}{T}\int_{t-T/2}^{t+T/2} dt\, n(x,t)n(x+\Delta x, t+\tau)$, where n is the measured signal and T is the duration over which each cross correlation is calculated. From the peak time lag and known separation distance Δx, the TDE velocity is calculated as $V_{\mathrm{TDE}} = \Delta x/\tau_p$. By moving the time window T and repeating the calculation, an ensemble of different realizations is used in calculating V_{TDE}, thus reducing the error. Denoting the total number of time windows as N, the TDE velocity can be obtained by finding the mean velocity from N time windows, allowing a measure of the statistical variation in V_{TDE}. Alternatively, the N correlation functions from all time windows can be averaged, and the mean velocity found from the peak of the average correlation function. We have tested both methods and they yield similar results; in the data presented here, we use the method that allows error bars to be calculated from the statistical variation.

The range of velocities that the TDE method can reliably infer is limited by the fact that the signals are discretely sampled over a finite time window. If we denote the length of the time window under consideration as T, then there is a maximum lag that can be inferred, $\tau_{max} = T/2$, which in turn specifies a *minimum* velocity magnitude $V_{min} = \Delta x/\tau_{max}$ that can be inferred. Discrete sampling implies that there is a *maximum* velocity magnitude that can be inferred, V_{max}

= $\Delta x/\Delta t$, such that fluctuations do not move a distance Δx in a time faster than Δt. Note that interpolation can be used to reduce the size of Δt significantly below the sampling period. In addition, the timescale τ_{decor} for the turbulence to decorrelate must be longer than the time window T so that the flow is approximately steady within T, because the TDE method relies on the Taylor frozen-flow hypothesis. Therefore, the range of inferable velocity magnitudes is bounded, with the range given by

$$2\frac{\Delta x}{\tau_{decor}} < 2\frac{\Delta x}{T} < |V| < \frac{\Delta x}{\Delta t}. \quad (1)$$

In Ref. [3], the TDE method was applied to test signals with known velocity fields in the presence of noise, showing that the TDE method reliably infers the mean velocity with magnitude greater than or equal to 0.2 $\Delta x/\Delta t$ with signal to noise ratios larger than 10, and reliably infers time-dependent flows if the flow varies sufficiently slowly ($f < 2/T$).

EXPERIMENTAL SET-UP AND RESULTS

The experiments are performed with the Controlled Shear De-correlation Experiment (CSDX) plasma device, which uses an azimuthally symmetric half-wavelength helicon antenna operating at 13.56 MHz with 1500 W of power (less than 20 W is reflected), with an Argon gas pressure of 3.0 mTorr. The plasma source radius is approximately 4.5 cm and is connected to a downstream cylindrical chamber of 10 cm radius and approximately 3 m length which is immersed in a solenoidal magnetic field of 1 kG (directed from the downstream end of the chamber toward the source). The field lines terminate on insulating surfaces in the plasma source and on the downstream end the field lines terminate on an insulating vacuum window, through which an axial view of the plasma column is recorded with a fast-framing camera. All

of the probe data shown here are obtained a distance 75 cm downstream from the exit plane of the plasma source, sampled at 1 MHz with azimuthal probe separation Δx = 0.5 cm. At 1 kG, the ion cyclotron frequency for Argon $f_{ci} = \Omega_{ci}/2\pi$ = 38 kHz, the sound speed $C_s = \sqrt{T_e/M_i} = 2.7\times10^5$ cm/s (using T_e = 3.0 eV), and ion-sound gyroradius $\rho_s = C_s/\Omega_{ci}$ = 1.1 cm; the density scale length (in the region of strongest gradient) $L_n = \left(d\ln n_0/dx\right)^{-1} \approx 3$ cm. A more detailed description of the plasma source and fluctuation characteristics can be found in the literature [10,11,12,13].

A four tip Mach probe is used to measure the plasma flow velocity, in both the parallel and perpendicular directions with respect to the axial magnetic field. The measurement is based on taking the ratio R_M of ion saturation currents from two 180-degree opposed probes. By rotating the Mach probe, R_M is measured as a function of the angle θ between the line connecting opposing probes and **B**. Following recent work by Shikama *et al.* [14], we then fit the data with a function of the form $R_M = \exp[K\sin\Delta\alpha/\Delta\alpha(M_{par}\cos\theta + M_{perp}\sin\theta)]$, where $\Delta\alpha$ is the acceptance angle of each probe tip, M_{par} and M_{perp} are used as fitting parameters, and we use Hutchinson's model of ion collection [15] with K = 1.34.

Fig. 1 shows the TDE velocity obtained from probes and fast-framing imaging, compared with the azimuthal fluid velocity measured with the Mach probe. Here, the Mach probe velocity $v_M = C_s(r)M_{perp}$ includes radial variation of C_s due to $T_e(r)$. Applying the TDE algorithm to the probe data yields a velocity profile shown by the red points. Images of the plasma viewed along an axial line-of-sight are obtained with a Phantom v.7.1 fast framing camera, using a frame rate of 67 kHz and spatial resolution of 64x64 pixels. We apply the TDE technique to 1500 frames of broadband emission intensity recorded by two pixels that image two azimuthally-separated

locations in the plasma. The results demonstrate that the TDE technique applied to imaging data agrees with the TDE velocity obtained from probes. We also observe that the TDE velocity is approximately 30% larger than the ion fluid velocity measured by the Mach probe. The results suggest that the fluctuations are advected by the plasma *ExB* flow and have an inherent phase velocity v_ϕ, which is presumably given by the dominant drift mode plasma-frame phase velocity driven by diamagnetic effects.

SIMULATION AND RESULTS

We can quantify the significance of the diamagnetic contribution to the TDE velocity using results from drift turbulence simulations with known advecting velocities and known pressure gradients, that is, with known *ExB* and drift wave phase velocities. Using a modified Hasagawa-Wakatani model [16] to describe a simple drift-wave system, we have applied to the TDE technique to fluctuations that naturally result from the turbulent simulation. The equations used in the simulation are given by

$$\frac{d\tilde{n}}{dt} + \tilde{V}_x \frac{dn_0}{dx} + \omega_{\|}\left(\tilde{n} - \tilde{\phi}\right) = D\nabla_{\perp}^2 \tilde{n}, \tag{2}$$

$$\frac{d\nabla_{\perp}^2 \tilde{\phi}}{dt} + \omega_{\|}\left(\tilde{n} - \tilde{\phi}\right) = \mu\nabla_{\perp}^4 \tilde{\phi}, \tag{3}$$

where the tildes denote fluctuating quantities, n and ϕ refer to the density and potential, μ is the normalized ion viscosity, the time scales have been normalized by C_s / L_n, and the spatial scales have been normalized by ρ_s. The "adiabatic parameter" $\omega_{\|} \equiv k_{\|}^2 v_{th_e}^2 / \upsilon_e$ quantifies the degree to which the Boltzmann relation $n_e = n_0 \exp\left(-e\phi / k_B T_e\right)$ is maintained via parallel electron dynamics (where v_{th_e} is the electron thermal speed and υ_e is the electron collision frequency).

Here, the total derivative includes advection by the turbulent velocity $\tilde{V} = -\tilde{\nabla}\tilde{\phi} \times \hat{z}$, and advection by an externally imposed mean flow V^0:

$$\frac{df}{dt} = \frac{\partial f}{\partial t} + \tilde{V} \cdot \tilde{\nabla} f + V^0 \frac{\partial f}{\partial y}, \tag{4}$$

where the modification to the original Hasegawa-Wakatani model is the addition of the second advection term $V^0 \partial_y f$. This slowly varying flow is given by $V_y{}^0(x,t) = U^0 \sin(k_x x)[1 + 0.5\cos(\omega_V t)]$, which is a shear flow in the *y* direction with steady and slowly oscillating components. This velocity field is intended to represent the advection of small-scale turbulent density fluctuations due to GAMs (the slowly varying component of V_y^0) and other large-scale shear which are important components of drift-wave turbulence in tokamaks [7]. The scale of the externally imposed shear flow is large, and is equal to the radial box size $L_x = L_y = 64\rho_s$ such that $k_x = 2\pi/L_x$; and the flow frequency is $\omega_V = 2\pi C_s / 10 L_n$.

The simulations are performed in a two-dimensional periodic box with 256 points used in each direction. The external flow parameter U_0 is set to 25.5, giving a strength of V_y^0 significantly stronger than the turbulent flow, but not so strong as to completely overpower the turbulence (RMS $V_y^0 = \left(3/2\sqrt{2}\right) k_x f_0 \sin(k_x x) \approx 2.66 \sin(k_x x)$, RMS $\tilde{V}_y = 0.715$). A snapshot of the turbulent density field is given in Fig. 2a. The TDE technique was applied to the density field at all radial and poloidal positions using an interpolation factor of 10 and poloidal separation of 1 ρ_s (well within the poloidal correlation length which is 5-6 ρ_s for all fluctuating quantities).

Snapshots of the inferred and actual poloidal velocity field are presented in Figs. 2b and 2c. In general, the macroscopic (large scale, slowly varying) components of the velocity are well

inferred in the regions where there is a significant mean velocity, but the technique does not accurately infer the small-scale components of the flow, or the flow as a whole in regions of small mean flow. To illustrate this conclusion in more detail, the inferred and actual mean poloidal flows are shown in Fig. 3. The black curve represents the time and flux-averaged total poloidal flow, and the red curve is the TDE-measured velocity. The slight offset between the two curves is most likely due to the fact that the TDE infers the lab-frame phase velocity, which is the sum of the (lab-frame) *ExB* velocity and plasma-frame phase velocity v_ϕ of the turbulence. This offset has a magnitude of approximately $0.5\rho_s C_s / L_n = 0.5 v_e *$, where the electron diamagnetic velocity is $\vec{v}_e * = \vec{\nabla} P_e \times \vec{B} / enB^2$, with the electron thermal pressure given by $P_e = nT_e$. The observed offset is approximately equal to the expected linear drift wave phase velocity $v_\phi = v_e * / (1 + k_\perp{}^2 \rho_s{}^2)$ when $V_y{}^0$ is equal to zero, because the dominant wavenumber of the density fluctuations is roughly $k_\perp = 2\pi / \lambda_\perp \sim \rho_s{}^{-1}$, as seen from Fig. 2a.

DISCUSSION AND CONCLUSIONS

The TDE technique applied to fluctuations measured with probes and applied to emission data from fast-framing imaging yield velocity profiles that are in good agreement. Based on the experiments and simulations presented here, we believe that the TDE-measured fluctuation phase velocity in the lab frame is given by the *ExB* drift velocity plus any plasma-frame phase velocity (caused by diamagnetic effects). Thus, there are limitations in using the 1D TDE technique to study particle transport, because the diamagnetic velocity component that is measured by the TDE method does not contribute to particle advection, which is caused by guiding center drifts. In addition, particle fluxes are driven by turbulent velocity fields, and correlation-based

algorithms such as TDE fail to infer rapidly varying velocity fields. The TDE technique can, however, be used to infer large-scale, slowly varying velocities, such as the equilibrium and slowly varying *ExB* flow within a flux surface in the scrape-off-layer of tokamaks. More advanced schemes such as 2D velocimetry [1] or orthogonal dynamic programming [17] may be more successful in overcoming some of the TDE limitations, and will be pursued in future work.

ACKNOWLEDGEMENTS

This research was performed under U.S. Department of Energy (DOE) grants DE-FG02-04ER54773 and DE-FG02-04ER54734. CH performed this research under appointment to the Fusion Energy Postdoctoral Research Program administered by the Oak Ridge Institute for Science and Education under contract number DE-AC05-00OR22750 between the U.S. DOE and Oak Ridge Associated Universities.

REFERENCES

[1] G. R. McKee, R. J. Fonck, D. K. Gupta, D. J. Schlossberg, M. W. Shafer, Rev. Sci. Instr. 75 (2004) 3490.

[2] J. L. Terry, S. J. Zweben, O. Grulke, M. J. Greenwald, B. LaBombard, J. Nucl. Mat. 337-339 (2005) 322.

[3] C. Holland, G. R. Tynan, G. R. McKee, R. J. Fonck, Rev. Sci. Instr. 75 (2004) 4278.

[4] Y. T. Chan, J. M. F. Riley, J. B. Plant, IEEE Trans. Acoust. Speech Signal Process. ASSP-29 (1981) 577.

[5] G. R. McKee, R. J. Fonck, M. Jakubowski, K. H. Burrell, K. Hallatschek, R. A. Moyer, D. L. Rudakov, W. Nevins, G. D. Porter, P. Schoch, X. Xu, Phys. Plasmas 10 (2003) 1712.

[6] K. Hallatschek, D. Biskamp, Phys. Rev. Lett. 86 (2001) 1223.

[7] Diamond, P. H., Itoh, S.-I., Itoh, K., Hahm, T.S., Plasma Phys. Controlled Fusion 47 (2005) R35.

[8] M. Jakubowski, R. J. Fonck, G. R. McKee, Phys. Rev. Lett. 89 (2002) 265003-1/4.

[9] G.R. McKee, R.J. Fonck, M. Jakubowski, K.H. Burrell, K. Hallatschek, R.A.Moyer, D.L. Rudakov, W. Nevins, G.D. Porter, P. Schoch, X. Xu, Phys. Plasmas 10 (2003) 1712.

[10] G. R. Tynan, A. D. Bailey III, G. A. Campbell, R. Charatan, A. de Chambrier, G. Gibson, D. J. Hemker, K. Jones, A. Kuthi, C. Lee, T. Shoji, M.Wilcoxson, J. Vac. Sci. Tech-A 15 (1997) 2885.

[11] J. George, *Experimental Study of Linear Resistive Drift Waves in a Cylindrical Helicon Plasma Device,* M.S. Thesis, Department of Mechanical and Aerospace Engineering, University of California, San Diego (2002).

[12] G. R. Tynan, M.J. Burin, C. Holland, G. Antar, N. Crocker, P.H. Diamond, Phys. Plasmas 11 (2004) 5195.

[13] M. Burin, G. Antar, N. Crocker, G.R. Tynan, Phys. Plasmas 12 (2005) 052320.

[14] T. Shikama, S. Kado, A. Okamoto, S. Kajita, S. Tanaka, Phys. of Plas. 12, 044504 (2005).

[15] I. H. Hutchinson, Plasma Phys. Cont. Fusion 47, 71 (2005).

[16] A. Hasegawa, M. Wakatani, Phys. Rev. Lett. 50 (1983) 682.

[17] G. M. Quenot, J. Pakleza, T. A. Kowalewski, Exp. Fluids 25 (1998) 177.

Figure Captions

Fig. 1: The velocity measured using the two-point correlation TDE technique from both probes and fast-framing imaging, compared to the ion fluid velocity measured with a Mach probe.

Fig. 2: Snapshots from the simulation of a) the density fluctuations, b) the actual velocity field and c) the TDE-inferred velocity field. The large-scale features are captured by the TDE method, but the small scale structure is lost.

Fig. 3: Comparison of the time and flux-averaged poloidal velocity from the simulation (black) with the TDE-inferred velocity (red). The slight offset is approximately equal to the phase velocity v_ϕ of the drift waves in the plasma frame.

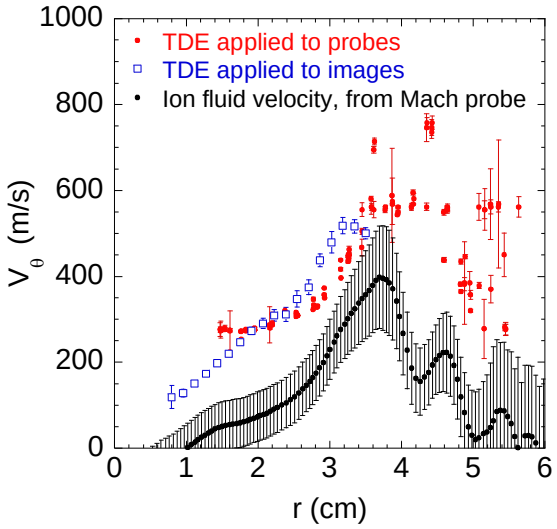
TDE applied to probes
TDE applied to images
Ion fluid velocity, from Mach probe
V_θ (m/s)
r (cm)
0
200
400
600
800
1000
0
1
2
3
4
5
6

Figure 1

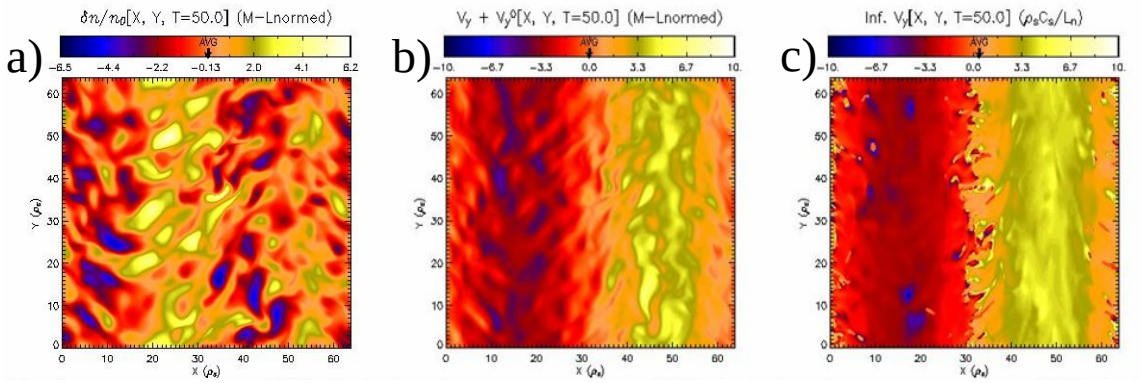
a)
$\delta n/n_0$[X, Y, T=50.0] (M−Lnormed)
AVG
−6.5 −4.4 −2.2 −0.13 2.0 4.1 6.2
b)
$V_y + V_y^0$[X, Y, T=50.0] (M−Lnormed)
AVG
−10. −6.7 −3.3 0.0 3.3 6.7 10.
c)
Inf. V_y[X, Y, T=50.0] ($\rho_s C_s/L_n$)
AVG
−10. −6.7 −3.3 0.0 3.3 6.7 10.
Y (ρ_s)
X (ρ_s)
0 10 20 30 40 50 60

Figure 2

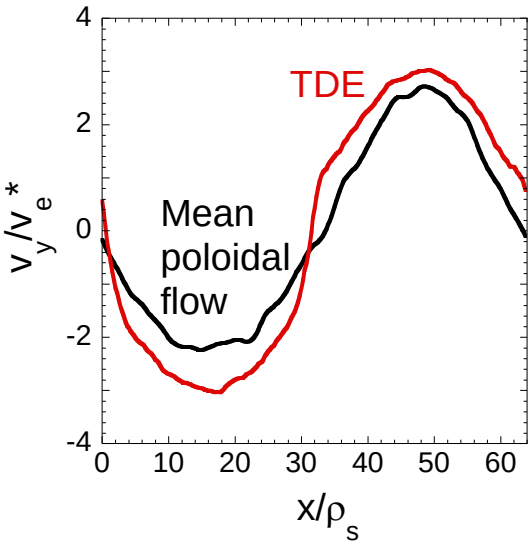

Figure 3

P2-25

Be-W alloy formation in static and divertor-plasma simulator experiments

M. J. Baldwin[(a)*], D. Buchenauer[(b)], R. P. Doerner[(a)], R.A. Causey[(b)], D. Nishijima[(a)], W.M. Clift[(b)] and K. Schmid[(c)]

(a) University of California at San Diego, CA 92093 USA

(b) Sandia National Laboratories, Livermore, CA 94550, USA

(c) Max-Planck Institut für Plasmaphysik, Garching Germany

Abstract

Collaborative Be–W interaction experiments conducted at UC-San Diego PISCES, and Sandia National Laboratories-Livermore, CA (SNL/CA), are reported. In the divertor-plasma simulator PISCES–B, W targets are exposed to Be seeded D_2 plasma in the temperature range 1070–1320 K. All targets reveal the formation of surface Be–W alloying. The alloy reaction rate is found to increase with surface temperature in the range 1023–1123 K in SNL vacuum-deposition phase formation experiments. In both sets of experiments the efficiency of surface alloying is found to depend on the availability of surface deposited Be. This availability is reduced by evaporation at high temperature, and also by plasma re-erosion in the case of PISCES–B targets. Surface analysis of targets using Auger electron spectroscopy (AES), wavelength dispersive x-ray spectroscopy (WDS), and x-ray diffraction (XRD) reveals $Be_{12}W$ as the dominant alloy composition where Be surface availability is optimal.

JNM Keywords: Beryllium, Beryllium Alloys and Compounds, Divertor Materials, First Wall Materials, Plasma-Materials Interaction, Tungsten, Tungsten Alloys and Compounds

PSI-17 Keywords: Beryllium, ITER, mixed materials, PISCES-B, tungsten

PACS: 52.40.Hf

Corresponding Author address: UCSD Center for Energy Research, 9500 Gilman Drive, La Jolla, CA 92093-0417 USA

E-mail address: mbaldwin@ferp.ucsd.edu

Presenting author: Dr. Matthew James Baldwin

Presenting author E-mail address: mbaldwin@ferp.ucsd.edu

1. Introduction

The current ITER design makes use of Be, W and C (graphite) plasma facing component (PFC) materials [1]. In the near future, JET will undertake 'ITER-like wall' experiments where a combination of these materials is also to be investigated [2]. In both devices, a Be first wall and a full or partial, W divertor will be common and the divertor plasma is expected to contain ionized Be due to first-wall erosion. In ITER, the fraction of Be in the plasma, $f_{\mathrm{Be}^+} \approx n_{\mathrm{Be}^+} / n_{\mathrm{e}}$, is expected to be in the range 0.01–0.10 [3], leading to an incident flux of ~100–1000 ML s^{-1} of Be on ITER divertor surfaces.

A real concern, where Be and W interact, is the formation of Be-W alloy. All Be–W alloy compositions have partial equilibrium liquid phases at or significantly below the melting point of W (3695 K) [4]. For dissolved Be levels ~5–67 at. %, a liquid phase component precipitates above ~2370 K . With increasing Be content, the stable alloy stiochiometries Be_2W, $Be_{12}W$ and $Be_{22}W$ are known to form, and these have molten phase components at ~2520 K, ~1780 K, and ~1600 K respectively**.** While the operational temperature range for ITER W PFCs is expected to be lower than this, at ~600–1300 K [5], localized hot regions and the effects of ELMs may see surface temperature excursions well into the Be–W partial liquid phase regime. Should Be transport into the W bulk be rapid enough that alloy formation is not limited to the near surface, a potentially serious problem that could affect reactor operation and PFC lifetime is possible.

2. Experiments

2.1. UC–PISCES

Plasma–materials interactions (PMI) studies are conducted in the PISCES–B divertor plasma simulator. PISCES–B produces intense deuterium plasmas (n_e~10^{18}–10^{19} m^{-3}, T_e~6–12 eV as measured by Langmuir probe) that can be seeded with controlled amounts of Be using a neutral Be atom source [3, 6]. Polished ITER grade W targets, 25 mm in diameter and 1 mm thick are exposed to high-flux (Γ_{D^+} =0.2–1.0 $\times 10^{23}$ ions $m^{-2}s^{-1}$) plasma over ~3600 s with f_{Be^+} set in the range 0.0005–0.008. Plasma conditions and target temperature, T_s, are kept fixed and a temperature range spanning 1070–1320 K was explored. Target bias regimes of floating and –75 V were used to explore the role of energetic ion bombardment. The energy of impacting ions is estimated from the target bias, $\langle E_{ions} \rangle \approx V_{bias} - 2kT_e$. Subsequent to exposure, targets are analyzed using scanning electron microscopy (SEM) and a wavelength dispersive x-ray spectrometer (WDS).

2.2. SNL Vacuum deposition experiments

Phase formation and reaction kinetics experiments are conducted in vacuum (<2×10^{-6} Torr) by depositing Be on to W targets (similar to those in section 2.1) with a high-temperature (up to 1750 K) effusion cell. A thermocouple and optical pyrometer are used to determine the surface temperature during both the deposition and a 1 hour pre-anneal at 1223 K. The average deposition rate for Be is measured on a cooled Si target. Full target surface coverage in Be (i.e. net Be deposition) was achieved with fluxes of

2×10^{19} $m^{-2}s^{-1}$ at 1023 K and 5×10^{19} $m^{-2}s^{-1}$ at 1123 K. An exposure conducted at 1223 K did not show complete Be coverage up to fluxes of 10^{20} $m^{-2}s^{-1}$.

3. Results and Discussion

3.1 PMI Be–W alloy formation (PISCES–B)

Fig. 1 shows a selection of W targets that were exposed to various Be seeded plasmas in PISCES–B. All of these targets show evidence of the formation of a Be–W alloy surface. By way of comparison, the images in Fig. 1 point to the availability of surface Be as a key factor in Be-W alloy production.

In the exposed-target cross-section of Fig. 1(a), a $Be_{12}W$ layer ~0.3 μm thick, has formed at the interface between the W surface and a ~5μm thick layer of Be surface deposits. This exposure was conducted at 1070 K with a floating target bias, so that the temperature and ion energy were low enough that the deposited Be did not evaporate, or erode by sputtering.

In comparison, Fig. 1(b) shows the surface of a target exposed under similar conditions except that the ion energy is ~60 eV. Despite the increased f_{Be^+} in this case, there is no apparent layer of deposited Be, as in Fig. 1(a). The absence of Be deposits can be explained by sputtering. Further, the loss of available surface Be results only small (~0.3 μm high) nucleation zones of Be–W alloy that are close to the composition $Be_{12}W$ distributed over a W rich surface as measured by WDS analysis. Cross-sectional analysis did not reveal significant Be below the surface.

Comparing the target cross-section in Fig. 1(c) to 1(a) reveals the effect of evaporation, which also acts to inhibit the formation of Be deposits. This target had a

higher exposure temperature of 1150 K and was also floating. The surface of the target has developed a $Be_{12}W$ alloy layer ~1 μm in thickness. This layer accommodates ~1×10^{22} m^{-2} Be atoms. The fluence of incident Be ions during plasma exposure was larger, 9.7×10^{22} m^{-2}. The difference is in reasonable agreement with the number of Be atoms that evaporate from a Be surface at 1150 K over 3600 s [7] (6.9×10^{22} m^{-2}).

Comparing Fig. 1(d) to 1(c), the even higher exposure temperature of 1320 K seems to be detrimental to alloy formation. The surface composition is below the stoichiometry for even Be_2W, and in spite of an expected increase in mobility for Be in the bulk, cross-sectional analysis revealed little evidence for any Be below the surface. On this target it seems likely that evaporation hindered the Be–W interaction; the evaporative flux of Be at 1320 K is 1.5×10^{21} $m^{-2}s^{-1}$ [7], much greater than the inbound flux of ~3.5×10^{19} $m^{-2}s^{-1}$ during plasma exposure. However, under the same conditions as in Fig. 1(d) but with ion bombardment at 60 eV, alloy nucleation zones are observed. Fig. 1(e) shows this, $Be_{12}W$ surface nucleation distributed over an almost identical surface to that of Fig. 1(d). The implantation of Be just beneath the surface, or additional energy of the incoming Be ions, is suspected as the contributing factor in this case.

A key message of Fig. 1 is that the availability of surface Be is paramount for Be–W alloy formation and that Be erosion by ions, and/or evaporation at high temperature, reduces availability. A surface particle balance model is useful for predicting the PMI conditions under which a deposited Be layer forms. Plasma deposited Be on the hot W surface can be eroded, redeposited, evaporated, or enter the bulk. Net Be layer growth is observed whenever the incident Be flux, $J_{\mathrm{in}}^{\mathrm{Be}}$, exceeds that lost, $J_{\mathrm{out}}^{\mathrm{Be}}$. These quantities are given by,

$$J_{\text{in}}^{\text{Be}} = f_{\text{Be}^+}\Gamma_{\text{D}^+}\left(1-R_{\text{r}}\right), \tag{1a}$$

$$J_{\text{out}}^{\text{Be}} = Y_{\text{D}\to\text{Be}}\Gamma_{\text{D}^+}\left(1-R_{\text{d}}\right)+ f_{\text{Be}^+}Y_{\text{Be}\to\text{Be}}\Gamma_{\text{D}^+}\left(1-R_{\text{d}}\right)+\Gamma_{\text{e}}\left(1-R_{\text{e}}\right)+\xi\left(T_{\text{s}}\right), \tag{1b}$$

where R_{r} is the reflection coefficient for Be on W, $Y_{\text{D}\to\text{Be}}$ and $Y_{\text{Be}\to\text{Be}}$ are the sputter yields for D^+ and Be^+ ions on Be, R_{d} and R_{e} are redeposition fractions for sputtered and evaporated Be, Γ_{e} is the evaporative flux of Be from the surface, and $\xi\left(T_{\text{s}}\right)$ is a loss flux into the bulk due to either diffusion [8] or chemical reaction [9]. The value of f_{Be^+} when Eqs. (1a)–(1b) are equated is the minimum 'critical' Be fraction in the plasma that will lead to the formation of a full Be deposited layer. At this critical value, alloy formation might be expected to be most efficient. With reference to the targets and PMI conditions in Fig. 1(a–e), these critical values, $f_{\text{Be}^+(critical)}$ are 0.2×10^{-4}, 0.0480, 1.0×10^{-4}, 0.0530 and 0.0050 respectively, calculated using sputter yield and reflection coefficients in [10], redeposition fractions in [3], and ignoring the reaction term, $\xi\left(T_{\text{s}}\right)$. In spite of the simplicity of the model and assumptions, somewhat good agreement is observed with the observations in Fig. 1. Only those targets where f_{Be^+} was greater than $f_{\text{Be}^+(critical)}$ (I.e. Figs 1(a) and (c)) had full alloy layer growth.

3.2 Be–W reactions in vacuum (SNL)

To investigate the growth of Be–W alloy layers over time, an atomic flux of Be was deposited onto W substrates at temperatures of 1023 K and 1123 K for 1 and 4 hours. The structure of the resulting layers was similar to those in Fig. 1(a), having net Be on the surface (full Be coverage) with a reacted layer between the Be and the W. Auger Line scans of a 3600 s exposed deposition target at 1123 K showed a uniform reacted layer ~1

μm thick of composition, $Be_{12}W$. A small amount of Be (3.5 at. %) was observed in the W below the layer, consistent with the solubility limit.

Fig. 2 shows the dependence of the reaction layer thickness on time and temperature, along with fits based on a diffusional behavior to the growth front. Also shown is a target grown for 3600 s at 1223 K, but for which only partial Be coverage was achieved. The line scan for this target indicated an alloy layer composition closer to $Be_{50}W_{50}$.

XRD was used to investigate the structure of the reacted alloy layers. Fig. 3 shows the intensity of two low-angle $Be_{12}W$ peaks ($2\theta = 17.306° \& 35.023°$) as a function of reacted layer thickness. The scaling of the higher intensity peak (2,2,0) correlates well with the reacted layer thickness indicative of uniform structural arrangement into the alloy phase throughout the reacted layer. For the target at 1223 K, which had low Be availability on the surface, the XRD peaks are almost absent.

4. Conclusion

W targets exposed at 1070–1320 K to PISCES–B Be seeded D_2 plasma reveal the formation of ~ Be_2W and $Be_{12}W$ surface alloys. At SNL, vacuum deposition experiments indicate increased $Be_{12}W$ reaction with temperature in the range 1023–1123 K. The reacted layer thickness in PISCES–B PMI and SNL experiments agree well over this temperature range when adequate surface Be availability is maintained. In PMI experiments, the loss of Be from the surface due to re-erosion and/or evaporation at high temperature, is found inhibit the formation of the alloy phase. AES, XRD and WDS surface analysis methods indicate that $Be_{12}W$ dominates when Be availability is adequate.

In ITER, a significant part of the W divertor area is expected to operate at around 600 K. At this temperature, the growth of reacted alloy should not be severe as suggested by Fig. 3. and data in the literature [9, 11, 12]. At higher temperature both the USCD and SNL Be-W experiments show that alloying proceeds most efficiently when the availability of surface Be is optimal. This availability, in terms of net layer growth of Be deposits, is reasonably predicted with the zero dimensional PMI surface model of section 3.1. At the ITER upper limit temperature of 1300 K, the present experiments show that it is difficult to achieve net Be layer growth due to evaporative loss. In ITER, where the plasma beryllium fraction and redeposition rates will be much greater, net Be layer growth will be sustained at considerably higher temperature than is achieved in the current experiments. This, coupled with transient high temperature thermal loads due to ELMing may lead to more rapid Be–W alloying effects. These phenomena are soon to be explored in PISCES–B using a new feature that allows target pulsing with transient heat loads [13] during plasma operation.

Acknowledgements

The authors gratefully acknowledge PISCES–B and SNL technical staff. This work is supported by USDoE contracts: DOE DE-FG03-95ER-54301 & DE-AC04-94AL85000.

References

[1] G. Federici, P. Andrew, P. Barabaschi, *et al*., J. Nucl. Mater. **313–316** (2003) 11.

[2] C. Grisolia, S. Rosanvallon, P. Coad, *et al*., Fusion Eng. and Design **81** (2006) 149.

[3] R. Doerner, M. J. Baldwin and K. Schmid, Physica Scripta **T111** (2004) 75.

[4] H. Okamoto, L. E. Tanner, in S. V. Nagendra Naidu, P. Ramo Rao (Eds), Phase Diagrams of Binary Tungsten Alloys, Indian Institute of Metals, Calcutta, 1991.

[5] G. Federici, R. A. Anderl, R. Andrew, *et al*. J. Nucl. Mater. **266–269** (1999) 14.

[6] M. J. Baldwin and R. P. Doerner, Nucl. Fusion **46** 4 (2006) 444

[7] D. R. Lide, CRC Handbook of Chemistry and Physics, Internet Version (2005)

[8] Linsmeir *et al.*, these proceedings

[9] E.Vasina, A. S. Panov, Russ. Metall. (Metally) 1 (1974) 119

[10] W. Eckstein, Calculated sputtering, Reflection and Range Values, Max–Planck Institut für Plasmaphysik Report 9/17, (1998)

[11] R. P. Doerner, M. J. Baldwin, R. A. Causey, J. Nucl. Mater. **342** (2005) 63

[12] C. R. Watts, International Journal of Powder Metallurgy **4** (3) (1968) 49

[13] J. Hanna *et al.* submitted to Rev. Sci. Instrum.

Figure captions

Fig. 1. (a–e) SEM images of W targets exposed to Be seeded D_2 plasma in PISCES–B. Compositional data provided by standardized WDS analysis at 5 kV. (a) and (e) are cross-sections, (b), (d) and (e) are the plasma exposed surfaces.

Fig. 2. Reaction layer thickness as a function of time, with fits based on diffusional reaction front behavior. The data point at 1223 K was not obtained under Be rich conditions.

Fig. 3. Scaling of (1,1,0) and (2,2,0) diffraction peaks with reaction layer thickness. The data point at 1223 K was not obtained with full Be surface coverage.

Fig. 2.

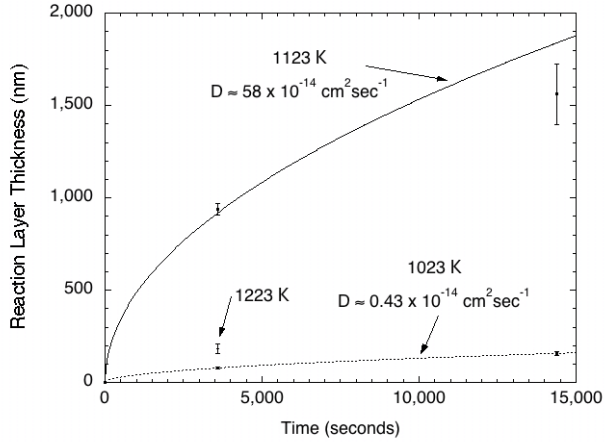
Reaction Layer Thickness (nm)
Time (seconds)
1123 K
D ≈ 58 x 10^-14 cm^2sec^-1
1223 K
1023 K
D ≈ 0.43 x 10^-14 cm^2sec^-1
2,000
1,500
1,000
500
0
0
5,000
10,000
15,000

Fig. 3.

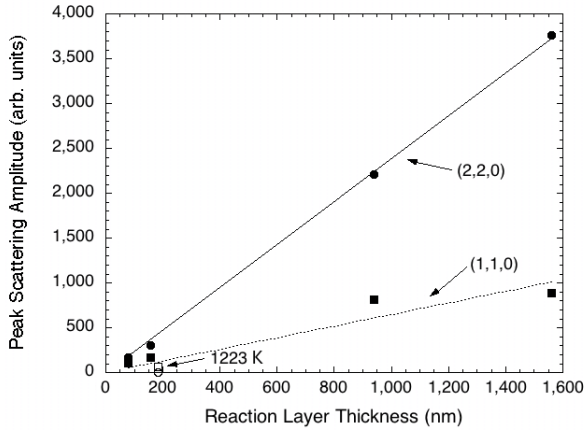
Peak Scattering Amplitude (arb. units)
Reaction Layer Thickness (nm)
(2,2,0)
(1,1,0)
1223 K
4,000
3,500
3,000
2,500
2,000
1,500
1,000
500
0
0
200
400
600
800
1,000
1,200
1,400
1,600

Fig. 1.

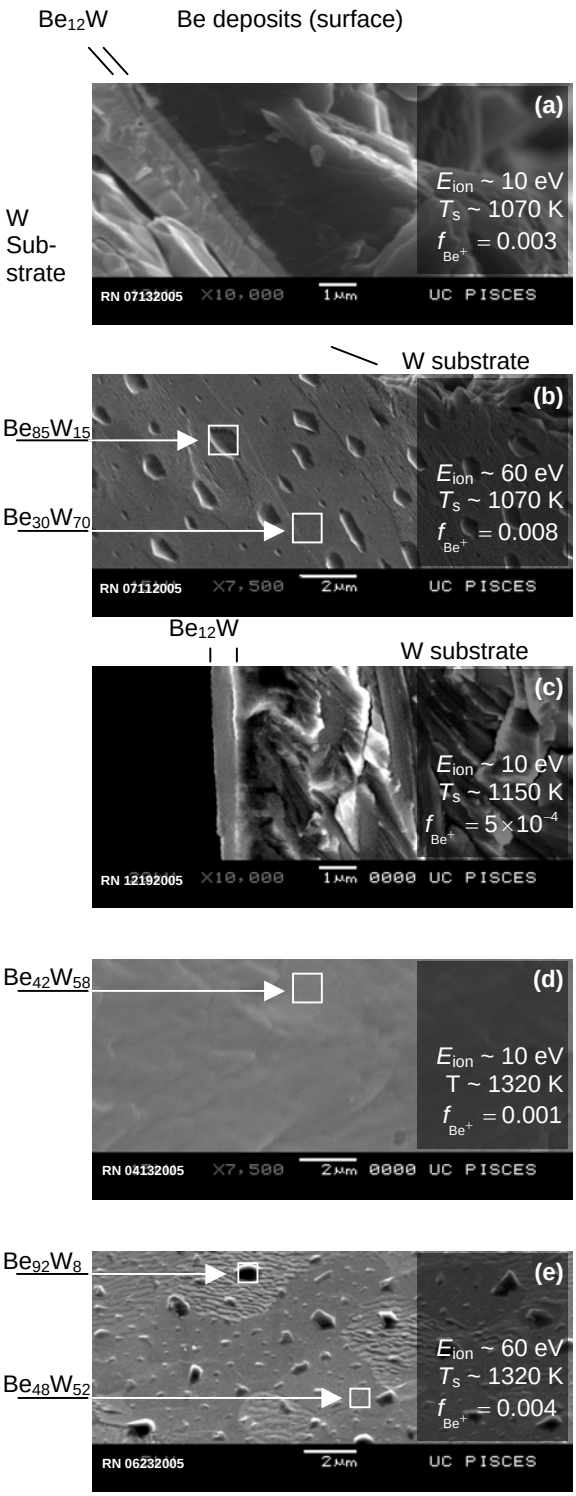
Be12W
Be deposits (surface)
W
Sub-
strate
(a)
Eion ~ 10 eV
Ts ~ 1070 K
fBe+ = 0.003
RN 07132005 X10,000 1µm UC PISCES
W substrate
(b)
Be85W15
Be30W70
Eion ~ 60 eV
Ts ~ 1070 K
fBe+ = 0.008
RN 07112005 X7,500 2µm UC PISCES
Be12W
W substrate
(c)
Eion ~ 10 eV
Ts ~ 1150 K
fBe+ = 5×10-4
RN 12192005 X10,000 1µm 0000 UC PISCES
Be42W58
(d)
Eion ~ 10 eV
T ~ 1320 K
fBe+ = 0.001
RN 04132005 X7,500 2µm 0000 UC PISCES
Be92W8
Be48W52
(e)
Eion ~ 60 eV
Ts ~ 1320 K
fBe+ = 0.004
RN 06232005 2µm UC PISCES